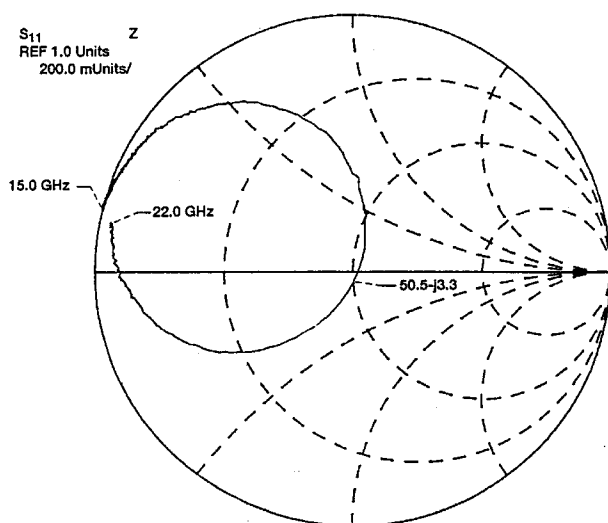**Figure 3** Experimental de-embedded return loss $|S_{11}|$ as a function of the notch depth d ($W = 0.792$ mm, $g = 0.343$ mm, $h = 0.254$ mm, $L = 4.928$ mm, $\varepsilon_r = 2.22$, frequency ≈ 20 GHz)

In Figure 4, the de-embedded input impedance Z_{in} at the reference plane b–b' for the above patch antenna with the optimum notch dimensions of $g = 0.343$ mm and $d = 1.63$ mm is shown. This figure shows that, at the design frequency of 20 GHz, the Z_{in} is $50.5 - j3.3$ Ω, which is very close to the desired 50 Ω. The same antenna configuration is analyzed using Ensemble™ software [6]. A computed result for Z_{in} is $49.0 + j9.5$ Ω, and the corresponding S_{11} is -25.0 dB. These results further validate our GCPW model for the notch region.

Last, to demonstrate the robustness of the above design, two more patch antennas operating at frequencies lower (7.0 GHz) and higher (33.0 GHz) than 20 GHz, and fabricated on substrates thicker (0.508 mm) and thinner (0.127 mm) than 0.254 mm were designed as per the above model, fabricated, and characterized. The de-embedded S_{11} obtained for the two patches are -22.3 and -24.8 dB, respectively. Thus, the

Figure 4 Experimental de-embedded input impedance as a function of the frequency ($W = 0.792$ mm, $g = 0.343$ mm, $d = 1.63$ mm, $h = 0.254$ mm, $L = 4.928$ mm, $\varepsilon_r = 2.22$, frequency ≈ 20 GHz)

versatility of our model is established for a wide range of substrate thicknesses and frequencies.

IV. CONCLUSIONS AND DISCUSSIONS

We have demonstrated a grounded CPW model and an accurate de-embedding technique to obtain an optimum width g and depth d, respectively, of a notch feed when a patch antenna is excited by a 50 Ω microstrip line. For a given patch, the optimum g is obtained when $Z_{0(GCPW)}$ of the notch region is 50 Ω and the optimum d is $0.331L$. The model is valid for wide range of substrate thicknesses and frequencies.

REFERENCES

1. C.A. Balanis, Antenna theory, analysis and design, Wiley, New York, 1997, 2nd ed., sect. 14.2.1.
2. R.C. Hansen, Phased array antennas, Wiley, New York, 1998, sect. 5.4.
3. J.-F. Zurcher and F.E. Gardiol, Broadband patch antennas, Artech House, Norwood, MA, 1995, sect. 2.2.1.
4. A.J. Zaman and R.Q. Lee, Design considerations for notch feeding of a patch antenna, USNC/URSI National Radio Sci Meeting Dig, June 1998, p. 10.
5. HP-EEsof microwave & RF design synthesis, series IV, LineCalc, Feb. 1994.
6. Ensemble version 5.1, Ansoft Corp., Jan. 1998.
7. NIST de-embedding software, program DEEMBED, revision 4.04, 1994.
8. R.B. Marks, A multiline method of network analyzer calibration, IEEE Trans Microwave Theory Tech 39 (1991), 1205–1215.
9. R.N. Simons and R.Q. Lee, On-wafer characterization of millimeter-wave antennas for wireless applications, IEEE Trans Microwave Theory Tech 47 (1999), 92–96.

APPLICATION OF THE HYBRID FDTD–FETD METHOD TO DISPERSIVE MATERIALS

Michael S. Yeung[1]
[1] Department of Manufacturing Engineering
Boston University
Boston, Massachusetts 02215

ABSTRACT: *The hybrid FDTD–FETD method developed by Wu and Itoh is extended to handle dispersive materials using a finite-element version of the recursive convolution method. For scattering by a plasma sphere with negative real permittivity, the hybrid FDTD–FETD method is found to be more accurate than FDTD, even when a mesh size four times smaller is used in the latter method.* © 1999 John Wiley & Sons, Inc. Microwave Opt Technol Lett 23: 238–242, 1999.

INTRODUCTION

The hybrid FDTD–FETD method developed recently by Wu and Itoh [1] combines the accuracy of the finite-element time-domain (FETD) method [2] in modeling curved surfaces with the computational efficiency of the finite-difference time-domain (FDTD) method [3]. However, the original hy-

brid FDTD–FETD method can only handle nondispersive dielectric materials.

In this letter, the hybrid FDTD–FETD method is extended to handle dispersive materials. Such materials are commonplace in electromagnetic scattering in the deep-ultraviolet (DUV) wavelength regime, such as the scattering of DUV light by a chromium photomask during the photolithography process used in the manufacturing of microchips. Two types of dispersive materials are considered, namely, an unmagnetized plasma, suitable for modeling DUV materials with negative real permittivity, and a Lorentz material, suitable for modeling DUV materials with positive real permittivity.

HYBRID FDTD – FETD FOR DISPERSIVE MATERIALS

Consider a dielectric object bounded by a curved surface S as shown in Figure 1. The computational domain is divided into a finite-element region Ω_{FE}, spanning the immediate vicinity of the two sides of S and bounded by a staircase surface Γ, and a finite-difference region Ω_{FD}, spanning the remaining part of the domain, including a one-cell-thick region $\Omega_{overlap}$ which overlaps Ω_{FE}.

Suppose that the electric field $\mathbf{E}^n$ is known throughout the domain at time step n. The magnetic field $\mathbf{H}^{n+1/2}$ at time step $n + \frac{1}{2}$ in Ω_{FD} including $\Omega_{overlap}$ can be updated by FDTD. The electric field $\mathbf{E}^{n+1}$ in Ω_{FD}, including the staircase boundary Γ but excluding $\Omega_{overlap}$, can then be updated by FDTD. The electric field $\mathbf{E}^{n+1}$ in Ω_{FE} including $\Omega_{overlap}$ is then found by solving a weighted-residual problem, using the electric field $\mathbf{E}^{n+1}$ on Γ as a boundary condition and the previous electric fields $\mathbf{E}^n$ and $\mathbf{E}^{n-1}$ as initial conditions. The process is then iterated in time.
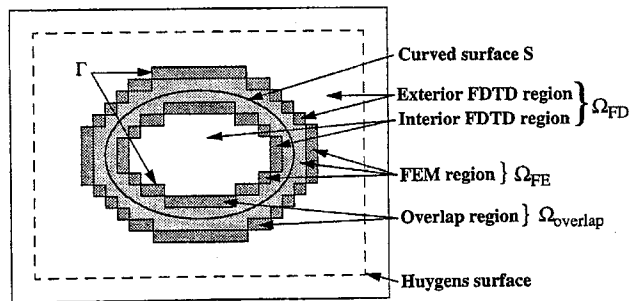
In a dispersive material, the electric displacement $\mathbf{D}$ and electric field $\mathbf{E}$ are related by

$$\mathbf{D}(\mathbf{r}, t) = \epsilon_0 \mathbf{E}(\mathbf{r}, t) + \epsilon_0 \int_0^\infty \chi(t') \mathbf{E}(\mathbf{r}, t - t') \, dt' \quad (1)$$

where $\chi(t)$ is the electric susceptibility. The case of an unmagnetized plasma is considered first. For such a material [4],

$$\chi^{\text{plasma}}(t) = \frac{\omega_p^2}{\nu_c} (1 - e^{-\nu_c t}) U(t) \quad (2)$$

where $U(t)$ is the unit step function and ω_p and ν_c are real constants. The weighted-residual problem in Ω_{FE} in the

Figure 1 Hybrid FDTD–FETD computational domain consisting of FDTD (Ω_{FD}) and FETD (Ω_{FE}) regions overlapping in a one-cell-thick region $\Omega_{overlap}$. Γ is the exterior boundary of Ω_{FE}

presence of the plasma is

$$\frac{\partial^2}{\partial t^2} \int_{\Omega_{FE}} \epsilon_0 \mathbf{E}^a \cdot \mathbf{E} \, d\Omega$$

$$= -\int_{\Omega_{FE}} \frac{1}{\mu} \nabla \times \mathbf{E}^a \cdot \nabla \times \mathbf{E} \, d\Omega$$

$$- \int_{\Omega_{FE}} \omega_p^2 e^{-\nu_c t} \mathbf{E}^a \cdot \mathbf{E} \, d\Omega$$

$$+ \int_0^\infty dt' \int_{\Omega_{FE}} \nu_c \omega_p^2 e^{-\nu_c t'} \mathbf{E}^a \cdot \mathbf{E}(t - t') \, d\Omega \quad (3)$$

where $\mathbf{E}^a$ is a test function and ω_p is zero outside the plasma.

Equation (3) is discretized in space by using the Whitney basis functions $\mathbf{W}_j$ [5] for field expansion and testing, and in time by using the Newmark–Beta scheme. Also, the convolution integral on the right-hand side of this equation is evaluated by assuming the electric field to vary linearly between successive time steps. This way, the following second-order accurate updating equation for the electric field in Ω_{FE} is obtained:

$$\overline{E}^{n+1} = \left([C] + \frac{\Delta t^2}{4} \{ [D] + [\chi_1] \} \right)^{-1}$$

$$\times \left[2 \left([C] - \frac{\Delta t^2}{4} \{ [D] + [\chi_1] \} \right) \overline{E}^n + \overline{\Psi}^n \right] - \overline{E}^{n-1} \quad (4)$$

where $\overline{E}^n$ is the vector of expansion coefficients at time step n and

$$[C]_{ij} = \int_{\Omega_{FE}} \epsilon_0 \mathbf{W}_i \cdot \mathbf{W}_j \, d\Omega \quad (5)$$

$$[D]_{ij} = \int_{\Omega_{FE}} \frac{1}{\mu} \nabla \times \mathbf{W}_i \cdot \nabla \times \mathbf{W}_j \, d\Omega \quad (6)$$

$$[\chi_1]_{ij} = \int_{\Omega_{FE}} \left(\frac{1 - e^{-\nu_c \Delta t}}{\nu_c \Delta t} \right) \omega_p^2 \mathbf{W}_i \cdot \mathbf{W}_j \, d\Omega. \quad (7)$$

Also,

$$\overline{\Psi}^n = \sum_{m=1}^{n-1} [\chi_2^{(m)}] \overline{E}^{n-m} \quad (8)$$

where

$$[\chi_2^{(m)}]_{ij} = \int_{\Omega_{FE}} 2 \left[\frac{\cosh(\nu_c \Delta t) - 1}{\nu_c \Delta t} \right] \omega_p^2 \Delta t^2 e^{-\nu_c m \Delta t} \mathbf{W}_i \cdot \mathbf{W}_j \, d\Omega. \quad (9)$$

Using the technique discussed in [4], $\overline{\Psi}^n$ can be computed recursively by

$$\overline{\Psi}^n = [\chi_2^{(1)}] \overline{E}^{n-1} + e^{-\nu_c \Delta t} \overline{\Psi}^{n-1}. \quad (10)$$

For a Lorentz material [6],

$$\chi^{\text{Lorentz}}(t) = \frac{(\epsilon_s - 1) \omega_0^2}{\sqrt{\omega_0^2 - \delta^2}} \text{Im}(e^{-\gamma t}) U(t) \quad (11)$$

where ϵ_s, ω_0, and δ are real constants and $\gamma = \delta - j\sqrt{\omega_0^2 - \delta^2}$. The updating equation for the electric field in Ω_{FE} has a form similar to Eq. (4), except that [χ_1] and $\overline{\Psi}^n$ in this equation must be replaced by $\mathrm{Im}[\chi_1]$ and $\mathrm{Im}(\overline{\Psi}^n)$, respectively. Also, ν_c in Eqs. (7), (9), and (10) must be replaced by γ, and ω_p^2 in Eqs. (7) and (9) must be replaced by $\gamma(\epsilon_s - 1)\omega_0^2 / \sqrt{\omega_0^2 - \delta^2}$.
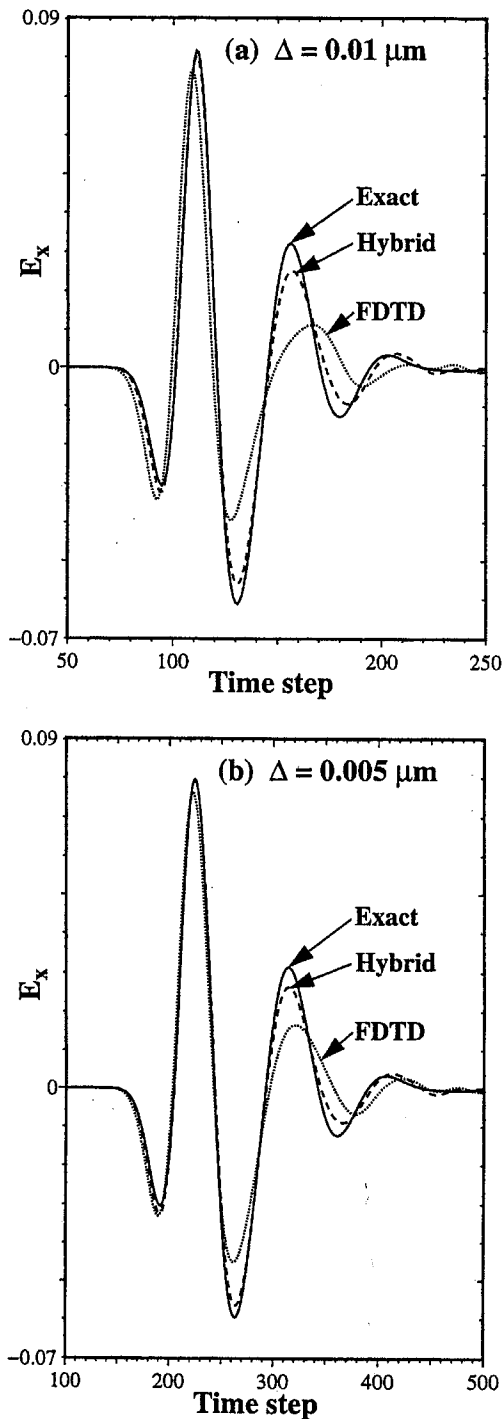
Figure 2 Scattered waveforms at a point one cell inside the outermost boundary and in front of a plasma sphere of radius 0.03 μm. Solid lines are exact results, dashed lines are results of hybrid FDTD–FETD, and dotted lines are results of FDTD. (a) $\Delta = 0.01$ μm. (b) $\Delta = 0.005$ μm

NUMERICAL RESULTS

The above formulation was applied to the electromagnetic scattering by a sphere of radius 0.03 μm. Two different meshes in Ω_{FD} were used, namely, a coarse mesh with $\Delta = 0.01$ μm and a fine mesh with $\Delta = 0.005$ μm, with $c\Delta t = 0.5\Delta$. The tetrahedral mesh in Ω_{FE} consisted of 5485 tetrahedra and 7158 edges for $\Delta = 0.01$ μm, or 16,681 tetrahedra and 21,682 edges for $\Delta = 0.005$ μm. The first-order Higdon absorbing boundary condition [7] was used on the outermost boundary of the computational domain, whose dimensions were 0.4 μm $\times$ 0.4 μm $\times$ 0.4 μm. A Huygens surface [8] located two cells inside the outermost boundary was used to excite the domain with a plane wave in the form of the time derivative of a Gaussian pulse:

$$\mathbf{E}_{\mathrm{inc}}^n = -\hat{x}3\sqrt{2e}\left(\frac{n}{n_0} - 1\right)e^{-[3(n/n_0-1)]^2} \qquad (12)$$

where $n_0 = 33$ or 66 for the coarse or fine mesh, respectively, and the factor $\sqrt{2e}$ is used to normalize the peak amplitude to unity.

For a plasma sphere, the parameters were chosen so that the refractive index of the sphere coincided with that of chromium, namely, $n = 0.85 + 2.01j$, at the DUV wavelength of $\lambda_1 = 248$ nm. The real part of the corresponding permittivity is negative. This gave $(\omega_p/\omega_1)^2 = 7.022$ and $(\nu_c/\omega_1) = 0.7914$, where $\omega_1 = 2\pi c/\lambda_1$. The scattered waveforms at a point one cell inside the outermost boundary and in front of the sphere are shown in Figure 2(a) and (b) for the coarse and fine meshes, respectively, together with the exact result of the Mie solution. It can be seen that the result of hybrid FDTD–FETD converged satisfactorily to the exact result as the mesh size decreased, whereas the result of FDTD converged much more slowly, especially at late times. The radar cross section at the wavelength λ_1 obtained by Fourier transformation is shown in Figure 3. Again, it can be
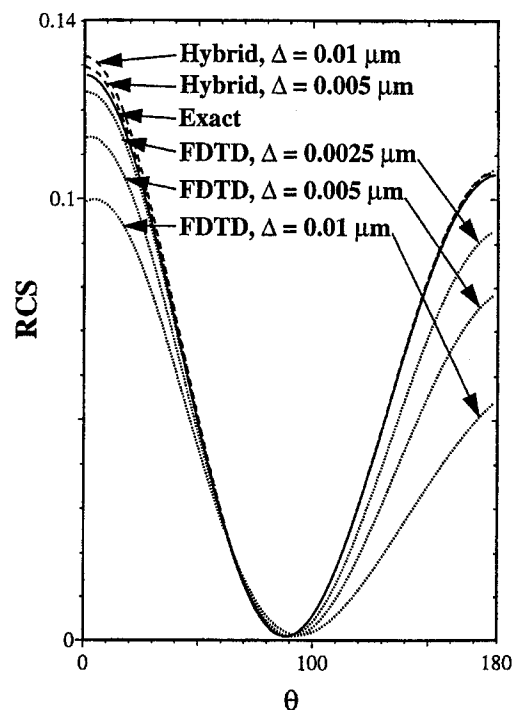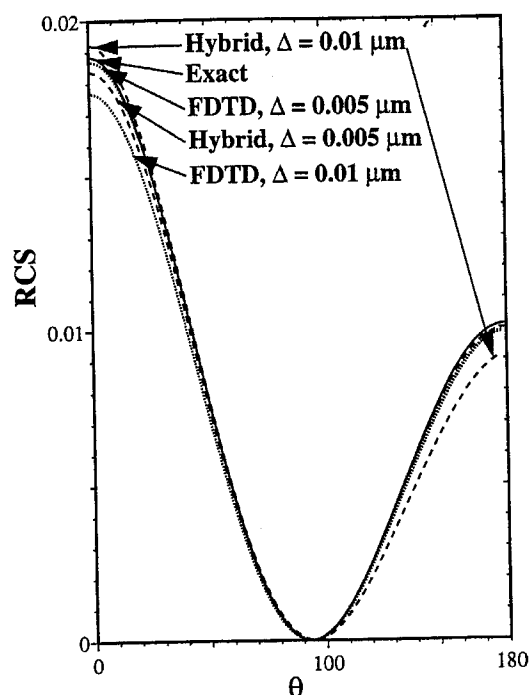

Figure 3 Radar cross section of the plasma sphere of Figure 2

seen that the result of hybrid FDTD–FETD converged satisfactorily to the exact result, whereas the result of FDTD converged much more slowly. Indeed, the FDTD result showed quite large discrepancies, even when an impractically small mesh size of 0.0025 μm, or roughly $\lambda_1/100$, was used.

For a Lorentz sphere, the parameters were chosen so that the refractive index of the sphere was $n = 1.8 + 0.4j$ at $\lambda_1 = 248$ nm, which is typical of antireflective materials used
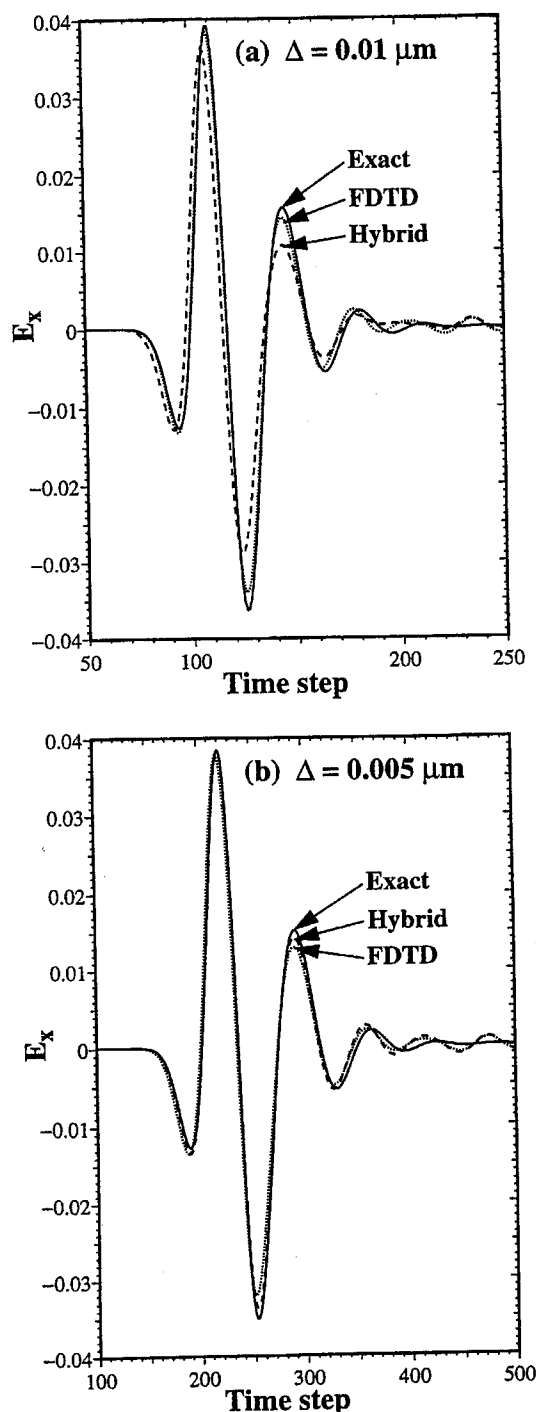
Figure 5 Radar cross section of the plasma sphere of Figure 4

for DUV photolithography. This gave $\epsilon_s = 2.709$ and $\delta/\omega_0 = 0.2885$, with ω_0 arbitrarily chosen to be $1.5\omega_1$. The scattered waveforms are shown in Figure 4(a) and (b) for the coarse and fine meshes, respectively. It can be seen that the results of hybrid FDTD–FETD and FDTD both converged satisfactorily to the exact result as the mesh size decreased. The radar cross section at the wavelength λ_1 is shown in Figure 5. Again, it can be seen that the results of hybrid FDTD–FETD and FDTD both converged satisfactorily to the exact result, and that the two methods are comparable in accuracy for the same mesh size.

CONCLUSIONS

The hybrid FDTD–FETD method of Wu and Itoh has been extended to handle dispersive materials. The validity of the formulation has been verified by comparison with exact results for scattering by plasma and Lorentz spheres. For a plasma sphere with negative real permittivity, it was found that hybrid FDTD–FETD with a mesh size of $\lambda_1/25$ is more accurate than FDTD with a mesh size of $\lambda_1/100$. For a Lorentz sphere, however, it was found that hybrid FDTD–FETD and FDTD are comparable in accuracy for the same mesh size. Since, in the DUV wavelength regime, dispersive materials with negative real permittivity are commonplace [9], and since such materials can only be modeled in the time domain by a plasma permittivity function, the hybrid FDTD–FETD method is much better suited to modeling curved surfaces than FDTD in the DUV wavelength regime.

Figure 4 Scattered waveforms at a point one cell inside the outermost boundary and in front of a Lorentz sphere of radius 0.03 μm. Solid lines are exact results, dashed lines are results of hybrid FDTD–FETD, and dotted lines are results of FDTD. (a) $\Delta = 0.01$ μm. (b) $\Delta = 0.005$ μm

REFERENCES

1. R.B. Wu and T. Itoh, Hybrid finite-difference time-domain modeling of curved surfaces using tetrahedral edge elements, IEEE Trans Antennas Propagat 45 (1997), 1302–1309.
2. J.F. Lee and Z. Sacks, Whitney elements time domain (WETD) methods, IEEE Trans Magn 31 (1995), 1325–1329.
3. K.S. Yee, Numerical solution of initial boundary value problems in isotropic media, IEEE Trans Antennas Propagat AP-14 (1966), 302–307.
4. R.J. Luebbers, F. Hunsberger, and K.S. Kunz, A frequency-dependent finite-difference time-domain formulation for transient propagation in plasma, IEEE Trans Antennas Propagat 39 (1991), 29–34.
5. A. Bossavit, Simplicial finite elements for scattering problems in electromagnetism, Comput Methods Appl Mech Eng 64 (1989), 299–316.
6. R. Luebbers and K. Kunz, FDTD calculation of scattering from frequency-dependent materials, IEEE Trans Antennas Propagat 41 (1993), 1249–1257.
7. R.L. Higdon, Absorbing boundary conditions for difference approximations to the multi-dimensional wave equation, Math Comput 47 (1986), 437–459.
8. R. Holland and J.W. Williams, Total-field versus scattered-field finite-difference codes: A comparative assessment, IEEE Trans Nucl Sci NS-30 (1983), 4583–4588.
9. A.K. Wong and A.R. Neureuther, Rigorous three-dimensional time-domain finite-difference electromagnetic simulation for photolithographic applications, IEEE Trans Semiconduct Manufact 8 (1995), 419–431.

MULTIBAND CHARACTERISTICS OF TWO FRACTAL ANTENNAS

Xu Liang[1] and Michael Yan Wah Chia[2]
[1] Center for Wireless Communications
Singapore Science Park II
Singapore 117674

ABSTRACT: *Experimental results show a multiband behavior for the Sierpinski gasket fractal antenna and the tree-like fractal antenna. Such behavior has been explained by the fractal structures of the antennas. We show that the matched frequencies possess a log-periodic behavior.*
© 1999 John Wiley & Sons, Inc. Microwave Opt Technol Lett 23: 242–245, 1999.

Spirals, cones, and log-periodic arrays are typical examples of frequency-independent antennas [1–3]. They have the fundamental property that their size relative to the operating wavelength remains invariable, which means that their shape is similar at different scales. Most fractal structures have a self-similar shape at different steps, and if they could be used in the design of radiating systems, they would be expected to have multiband operation [4–6]. In this paper, the authors introduce a new type of fractal antenna called tree-like antennas. Experimental results are shown to explain the multiband behaviors of the Sierpinski gasket antenna and the tree-like antenna.

The first fractal structure is the Sierpinski gasket fractal antenna. It is printed over a thin dielectric substrate ($\varepsilon_r =$

2.17, $h = 1$ mm) and mounted over a 50×50 cm conductor ground plane. The fractal dimension of this antenna is $\log 3 / \log 2 = 1.585$. Four typical antennas are made, and the experimental results of the VSWR are shown. It can be discussed as follows.

1. Figure 1(b) shows that the antenna in Figure 1(a) possesses a wideband property (actually, it is the well-known bow-tie antenna). When it is constructed as the fractal structure of basic step 1, shown in Figure 2(a), the antenna is matched at one point (resonance frequency $f_1 = 1.84$ GHz in the lower band, while in the upper band, it presents wideband behavior which is similar to that shown in Figure 1(b). This may be explained by the construction of the antenna. The fractal structure changes the current distributions of the original triangle; however, the triangle A_0OB_0 is still a bow tie with a small size which possesses a wideband property, and it seems that the height H of the antenna approximately equals the half wavelength of the matching point.
2. If this fractal process is carried out continuously, the original matching point still remains, and new matching points appear correspondingly. The antenna in Figure 3(a) is constructed with four iterations. That is, the Sierpinski gasket appears at four different scales within the main structure. They are A_1OB_1, A_2OB_2, A_3OB_3, and AOB, with heights of 8.1, 4.05, 2.03, and 1.02 cm, respectively. This antenna is matched at four bands, shown in Figure 3(b). It is clear that one fractal iteration structure forms one matching point. So it can be concluded that the number of matching points is equal to that of the iterations of the fractal antenna structure.
3. All of these matching points clearly show a log-periodic behavior; the log period is about a factor of 2 because the construction process is a scaled down version by a factor of 2.
4. The four iteration structures of the antenna in Figure 3(a) retain the same shape under certain scaling transformations. Therefore, the radiation patterns at all of these matching points are similar to each other [5].
5. Up to now, it has been known that the Sierpinski gasket presents multiband behavior. But is that true for any fractal structure? Our result shows otherwise. Figure 4 presents the measured results of the Sierpinski carpet. The feedpoint is any one of the four corners of the carpet. There is no difference between the two cases of steps 2 and 3. That is so for the feedpoint at the midpoint of either side of the carpet. The reason is that, for the gasket, the common vertex of two contiguous triangles is one point, while it is not for the carpet. In other words, the current distributions of the Sierpinski gasket antenna at different steps are different, but do not vary for the Sierpinski carpet antenna.
6. The Sierpinski gasket fractal antenna is similar to the log-periodic dipole array in some sense. The difference lies in that the former is a multiband antenna, while the latter is a broadband antenna.

The second fractal structure is the tree-like antenna. The basic geometry of the antenna is constructed as follows. Choose a length as our initial line, and divide it into three